Reprint from *RSC Advances*, **4**, 14962 (2014)

Formation and dynamics of partially wetting droplets in square microchannels

Bibin M. Jose and Thomas Cubaud

Department of Mechanical Engineering, Stony Brook University, NY, 11794 USA

Table of contents entry

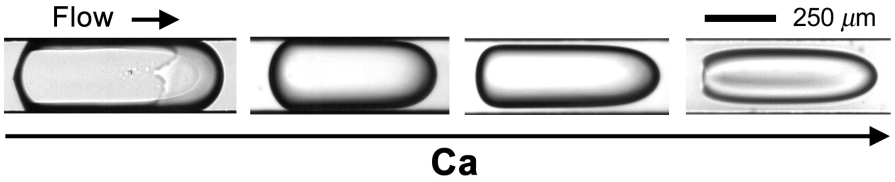

Droplet motion and dynamic wetting transitions are experimentally investigated over a wide range of viscosities and flow rates in square microchannels

Abstract

We experimentally study the production and evolution of partially wetting droplets as a function of the dynamic advancing contact angle and the viscosity of the external phase in microchannels. The natural spreading properties of immersed droplets are measured using high-speed goniometry and their forced spreading behaviors are probed in confined microgeometries. Low- and high-viscosity microfluidic segmented flows are generated by focusing water in a continuous phase of silicone oil using square microchannels. The shape and stability of the lubricating film between droplets and channel walls permit the classification of typical flow regimes, including wetting, thin film, thick film, and constant film thickness. Hysteretic partially wetting systems are shown to exhibit two modes of droplets formation, namely dripping and rivulet. Small-scale multiphase flows are investigated as a function of capillary number, droplet size, concentration, and velocity. We also discuss the occurrence of dynamic wetting transitions and stick-and-slip motion of microfluidic droplets. This study shows the possibility to control droplet dynamic wetting behavior with flow rates of injection in microfluidic platforms.

1. Introduction

Multiphase transport in porous media is a topic of significant interest in many areas of science and engineering, such as ground water hydrology,[1-3] oil recovery,[4-8] water-oil filtration,[9-11] and fuel cells.[12] Examples of basic flow operations through permeable micro-structured solids include fluid displacement by another fluid (*e.g.*, enhanced petroleum recovery) and multiphase flows where fluids are simultaneously injected through a membrane (*e.g.*, filtration). Depending of fluids properties and flow parameters, hydrodynamic destabilization processes, such as Saffman-Taylor[13] and Rayleigh-Plateau[14] instabilities, can alter fluid recuperation operations and materials can accumulate or remain trapped in the medium.[3]

As a porous medium typically consists of a complex solid matrix composed of a random network of interconnected pores through which fluid can flow, a modeling strategy consists in approximating the pore geometry

with two parallel plates and examine Hele-Shaw flows. Likewise, connecting throats between pores can be modeled with polygonal capillaries to capture the non-axisymmetric characteristics of small passages.[15] Micro-scale multiphase flows in basic plane and compact geometries have recently been examined using microfluidic devices,[16-25] in particular for confined droplet flows[26] in the context of applications ranging from materials synthesis[27] to bioengineering.[28] In these systems, similar to drainage[29] and imbibition[30] processes during fluid displacement in porous media, multi-components fluids, such as emulsion and foam, are strongly dependent on fluid wetting characteristics.[31]

Wetting properties are primarily determined with the static contact angle θ made at the intersection of a solid substrate and a fluid/fluid interface at rest.[32-34] The static contact angle is used to classify partially wetting fluids when $\theta < \pi/2$ and partially non-wetting fluids when $\theta > \pi/2$. The case where fluids adopt an angle $\theta \sim 0$ is referred to as complete wetting and leads to the formation of a metastable thin film covering the substrate.[35] The case associated with $\theta \sim \pi$ is labeled as complete non-wetting and, on a plane surface, droplets take a spherical shape with negligible wetting contact area. Wetting transitions and interfacial morphologies have been examined in detail for liquid-gas interfaces as a function of temperature[36, 37] and for various mechanical and chemical surface patterning.[38-41] For liquid-liquid interfaces,[42-47] relatively less is known on the influence of contact line velocity and wetting angle on the dynamics of droplets in confined microgeometries.

In general, the confinement of the capillary surfaces leads to a non-trivial influence of wetting phenomena on flow dynamics in part due to (a) the hysteretic nature of contact line motion,[48] (b) the possibility for wetting lines to align with the flow direction and form saw-teeth shapes,[49] (c) dewetting processes of thin films,[50] (d) Marangoni effects caused by surfactant,[51] and (e) surface heterogeneities.[52] Hence, there is a need to improve our basic understanding of the influence of external flows on the dynamic wetting properties of droplets in microchannels.

In this study, we experimentally measure the natural spreading properties of model fluid pairs made of pure water and silicone oils of various viscosities and probe their forced dynamic wetting properties in square microchannels. In particular, we measure the natural spreading velocity at the wetting/non-wetting transition of immersed droplets using high-speed goniometry and use this information to characterize the influence of the capillary number during droplet transport in microchannels. A simple method to generate droplets of various sizes is used to investigate the influence of the carrier fluid viscosity on droplet flow regimes. Hysteretic partially wetting systems are shown to exhibit two modes of droplets generation, including dripping and rivulet. The evolution of the lubricating film thickness with the capillary number permits the classification of flow regimes depending on droplet size, concentration, and velocity. Typical forced wetting phenomena are discussed in relation with a comprehensive series of experimental measurements.

2. Materials and Methods

The experimental setup consists of (a) a hard microfluidic platform used to continuously generate water droplets in silicone oil at externally imposed velocities and (b) a goniometer apparatus used in conjunction with a trans-

parent cell for examining the natural spreading properties of water on glass in an external phase of viscous silicone oil.

2.1. Microfluidic setup

Non-deformable microchannels are fabricated using double-side-polished silicon pieces that are etched through their entire thickness h = 250 μm using deep reactive ion etching and then sandwiched between two borosilicate glass slides using anodic bonding.[53] To visualize microflows, a microfluidic module is placed on top of an inverted microscope equipped with high-speed camera and a fiber optic bundle is located above the microchannel to provide illumination. Fluids are injected into the device using high-pressure syringe pumps.

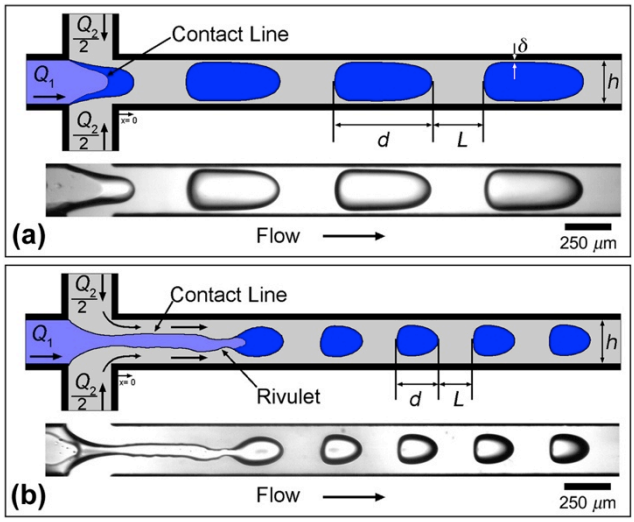

Fig. 1 Micrographs and schematics of two regimes of droplet formation using symmetric hydrodynamic focusing sections: (a) dripping regime, where droplets are produced at the fluid junction, α_2 = 0.48, and (b) rivulet regime in which droplets are emitted at the tip of a wetting tongue, α_2 = 0.77. Fluid pair: W-500cS

The microfluidic design comprises a fluid focusing section made of two channels intersecting at right angles to generate droplets and an outlet observation channel to examine multiphase flows morphology and dynamics [Fig 1]. All channels are square in cross-section with a width h. The droplet phase $L1$, having viscosity η_1, is introduced through the central inlet channel at flow rate Q_1 and the continuous phase $L2$ of viscosity η_2 is symmetrically injected from the side-channels with a total flow rate Q_2. Flow rates for Q_1 typically span between 1 and 200 μL/min and from 1 to 400 μL/min for Q_2. The flow rate ratio $\varphi = Q_1/Q_2$ ranges between 10^{-2} and 10^{1}. The film thickness δ around the droplet is measured at the point of minimum thickness. The length of the droplet is measured as d and the spacing between two successive droplets as L. A particularity of wetting systems is their hysteretic nature and here we observe the existence of two droplet production modes for similar injection conditions, namely a dripping regime, where droplets are produced at the fluid junction [Fig. 1(a)], and a rivulet re-

gime, where droplets are emitted from the tip of a wetting tongue that is mainly aligned parallel to the flow direction [Fig. 1(b)].

2.2. Fluid properties

Fluid Pair	γ_{12} (mN/m)	χ	θ_{Am} (deg)	Symbol
W-1cS	41	1.2	65	○
W-5cS	32	2.2×10^{-1}	66	□
W-20cS	33	5.3×10^{-2}	89	△
W-50cS	34	2.1×10^{-2}	91	▽
W-100cS	35	1.0×10^{-2}	105	◁
W-200cS	35	5.2×10^{-3}	113	▷
W-500cS	35	2.1×10^{-3}	137	✧
W-1000cS	35	1.0×10^{-3}	158	◊
W-10000cS	35	1.0×10^{-4}	180	◇

Table 1 Properties of the fluid pairs water and silicone oils, where γ_{12} (±1 mN/m) is the interfacial tension, $\chi = \eta_1/\eta_2$ is the viscosity ratio, and $\theta_{Am} = \theta(V)$ is the measured dynamic advancing contact angle for the velocity $V = 250$ μm/s.

The properties of the fluid pairs investigated in this study are displayed in Table 1. The droplet phase $L1$ is composed of pure water and the external phase $L2$ is made of conventional polydimethylsiloxane oils, *i.e.*, PDMS or silicone oil, of different viscosities. Fluid pairs are labeled based on the kinematic viscosity of the silicone oil, for instance the fluid pair W-100cS refers to water in an external phase of silicone oil having a kinematic viscosity ν_2 = 100 cS. Parameters of interest include the dynamic viscosity ratio $\chi = \eta_1/\eta_2$ and the fluid pair interfacial tension γ_{12}, which is measured using the combined capillary rise method.[54] Typical values of γ_{12} are found to plateau around 35 mN/m, albeit a value of 41 mN/m is systematically measured for fluid pair W-1cS. The kinematic viscosity of $L2$ is varied over four decades (from 1 to 10^4 cS) and the viscosity of the droplet phase $L1$ remains constant. From low to high viscosity, the specific gravity of silicone oils slightly varies from 0.812 to 0.974. Another important parameter is the contact angle θ made by water droplets in a continuous phase of silicone oil on the microchannel walls. In the presence of a very viscous environment, however, the relaxation time for the contact angle θ to reach its static equilibrium value θ_E can be very long (i.e., a few days), therefore the relevant wetting angle to characterize droplets dynamics in confined microflows is the dynamic advancing contact angle θ_A, which depends on the contact line velocity V. Typical values of the minimum advancing contact angle θ_{Am} based on the slowest injection velocity of $L1$ into the microchannel $V = Q_1/h^2 \sim 250$ μm/s are measured using the go-

niometer apparatus and are reported in Table 1. Data show that θ_{Am} depends on the viscosity of the external phase with an effective dynamic transition from partially wetting droplets to partially non-wetting droplets that occurs for fluid pairs W-20cS and W-50cS.

2.3. Dynamic Contact Angle Measurements

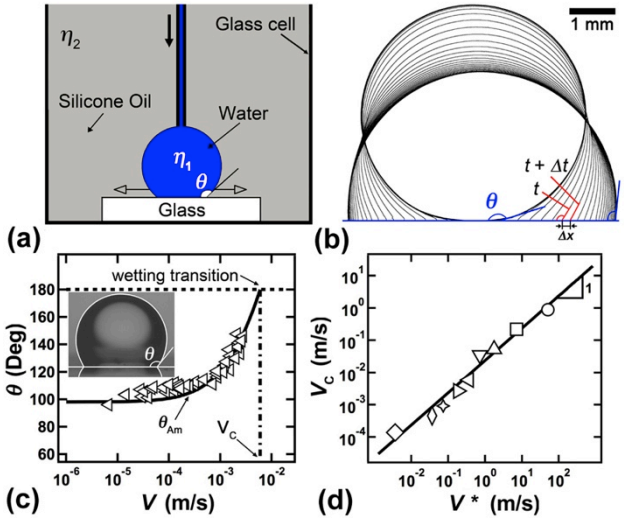

Fig. 2 (a) Scheme of apparatus for immersed droplet spreading experiment. (b) Superimposition of droplet contour plots during natural spreading, Δt = 25 ms (c) Evolution of advancing contact angle as a function of velocity, fluid pair: W-100cS. Solid line: $\theta = (\theta_0^3 + \omega V)^{1/3}$ with $\omega = 8.2 \times 10^8$ and $\theta_0 = 98°$. Dashed line: $\theta = 180°$. Dash-dot line: predicted velocity at which contact angle is expected to reach π. (d) Critical velocity V_C as a function of capillary velocity $V^* = \gamma_{12}/\eta_2$ for fluid pairs investigated. Solid line: $V_C = Ca_c V^*$, with $Ca_c = 2.4 \times 10^{-2}$.

To determine the natural spreading dynamics of water droplets on borosilicate glass when immersed in a phase of silicone oil, we use a method that combines goniometry and high-speed imaging. The glass walls of the microchannel are exposed to high temperature during the anodic bonding microfabrication step, which makes them strongly hydrophilic. To reproduce the surface properties of the microchannel glass walls, the borosilicate glass surface used for immersed natural spreading experiment is treated at 400º C for 1 hour and allowed to return to room temperature inside the oven to limit exposure to air contamination. Using a transparent cell, water droplets are then deposited onto the glass surfaces in a bath of silicone oil using a capillary tube connected to a syringe pump [Fig. 2(a)]. This technique permits the slow generation of a water droplet at the end of capillary tube. When the thin film of silicone oil between the droplet and the solid walls breaks, water spreads on the glass substrate while displacing the oil. The motion of the liquid-liquid interface is recorded with a spatial resolution of 10 μm and temporal resolution up to 2000 frames per second using a high-speed camera fitted to the goniometer. As the droplet spreads, the contact line velocity V decreases with time t and the apparent advancing contact angle θ_A

decreases from π to θ_E [Fig. 2(b)]. In the case of forced spreading experiments in microchannels however, the value of the equilibrium static angle θ_E is not the most relevant parameter compared to the dynamic advancing contact angle $\theta_A(V)$.

To correlate velocities V and contact angles θ, each image imported from the camera is assigned a contact angle and a coordinate for the three phase contact line. During the experiment, we focus on the plane where the contact line is farthest from the center of the droplet to avoid misinterpretation of the contact angle. The reflected image on the glass is used to locate the contact line on the line of reflection. Taking two images that are Δt apart, we measure the displacement Δx of the contact line and assign a velocity as $V = \Delta x/\Delta t$. Similarly, we assign a mean contact angle as $\theta = (\theta_t+\theta_{t+\Delta t})/2$ from the same pair of images used for calculating velocity. We assign the mean contact angle θ to the contact line velocity V [Fig. 2(b)]. These data are used to generate a typical graph of the dynamic contact angle as a function of velocity [Fig. 2(c)]. The critical velocity V_C for which the contact angle tends to π (*i.e.*, dynamic non-wetting transition) is extrapolated using the Cox-Voinov[47, 55] relation $\theta^3 = \theta_0^3 + \omega V$, where θ_0 and ω depend on the fluid pair. Although Cox-Voinov law describes contact angle for $\theta < 135°$ in the limit of low capillary number $Ca << 1$, this law is useful for predicting the critical velocity V_C at which the contact angle $\theta \rightarrow 180°$. Series of experiments are repeated for each fluid pair, and the resulting critical velocities V_C are compared with their capillary velocity counterpart $V^* = \gamma_{12}/\eta_2$ [Fig. 2(d)]. Since all droplets are made of pure water, the capillary velocity is calculated based on the viscosity of the external phase η_2. Here, data suggest a simple relationship $V_C = Ca_c V^*$ with the critical capillary number $Ca_c = 2.4\times10^{-2}$. Since the interfacial tension of each fluid pair is similar, the critical velocity V_C scales with the viscosity of the external phase as $V_C \sim 1/\eta_2$. The determination of V_C and Ca_c for the dynamic non-wetting transition of droplets yields useful quantitative information about droplet dynamics inside microgeometries.

3. Results and Discussion

3.1. Film stability and capillary number

A variety of multiphase flow regimes are observed as the capillary number $Ca = \eta_2 V/\gamma_{12}$, where V is the droplet velocity, ranges from 10^{-4} to 10^{1} due to the stability and shape of the intercalating film between droplets and the walls. The evolution of the thickness of the wetting layer is denoted with δ and displayed as a function of the capillary number Ca in Fig. 3(a). For very low Ca, hydrodynamic forces are negligible compared to surface tension forces and the system adopts a wetting state where droplets make direct contact with the confining walls, which is experimentally visible due to the presence of contact lines. When the capillary number $Ca > 10^{-3}$, the film becomes thicker and dynamically more stable to the formation of dewetting patches. As a result, lubricated droplets are more steadily produced. In the thin film regime, the droplet size exhibits a relatively weak dependency on the capillary number Ca. This effect can be seen when fixing a constant flow rate ratio $\varphi \sim Q_1/Q_2$ while

increasing the absolute flow velocity $J \sim (Q_1+Q_2)/h^2$. In this regime, measurements suggest that for fixed flow rate ratio φ, the droplet size d varies with the capillary number Ca according to $d/h \sim \mathrm{Ca}^a$, with $a = -0.2$ [Fig. 3(b)]. As viscous effects become more prominent when Ca increases, smaller droplets are produced in the thin film regime. We define the thick film regime when $\mathrm{Ca} > 10^{-1}$ as optical measurements of δ allow for directly examining its evolution, which scales as $\delta \sim \mathrm{Ca}^{2/3}$ until Ca reaches unity and a constant film thickness $\delta/h \sim 0.11$ is observed [Fig. 3(a)]. By contrast to the thin film regime, in thick film regime, the film thickness δ is significant and the droplet size d slightly increases with Ca. Indeed, at fixed φ, the droplet size grows with the capillary number as $d/h \sim \mathrm{Ca}^{0.07}$ [Fig. 3(c)]. This very minor variation in the droplet size can be attributed to the additional confinement of the droplets due to the lubricating continuous phase at the walls.

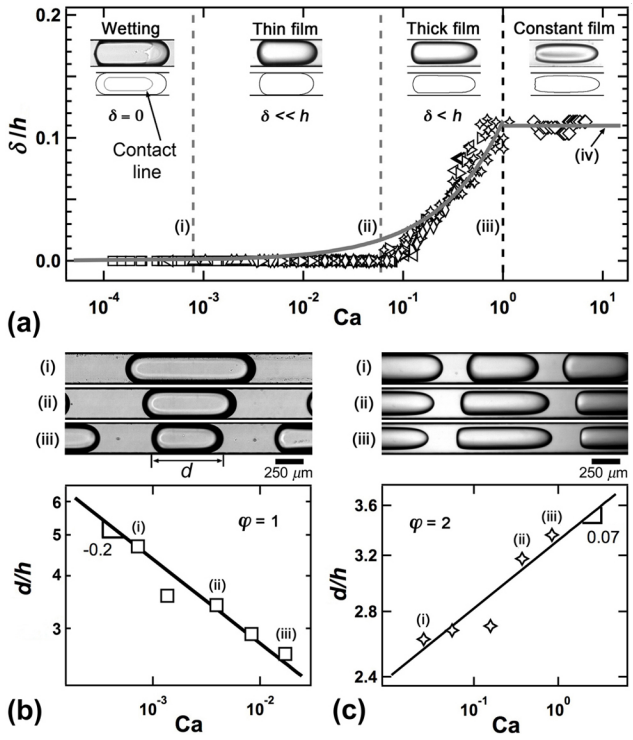

Fig. 3 (a) Film thickness normalized with the channel width δ/h as a function of capillary number Ca. Solid line: $\delta/h = \Omega\mathrm{Ca}^{2/3}$, with a cut-off at $\delta/h = 0.11$ and $\Omega = 0.11$. (b) Droplet size decreases with capillary number in the wetting and thin film region where the film thickness is negligible, solid line: $d/h = 1.1\mathrm{Ca}^{-0.2}$. (c) Droplet length increases due to the increase of film thickness in the thick film region, solid line: $d/h = 3.3\mathrm{Ca}^{0.07}$.

3.2 Dripping regime

An important feature of segmented microflows is the conservation of the linear aspect ratio d/L of the multiphase flow, which is found to be directly proportional to the flow rate ratio according to $d/L = c\varphi$, with $c = 1.75$ for capillary numbers Ca ranging between 10^{-4} and 10^{1} [Fig. 4(a)]. This property results from mass conservation applied to a linear unit cell of the flow over a period of droplet emission since the scalings $d \sim Q_1/h^2$ and $L \sim Q_2/h^2$

suggest direct proportionality of d/L with φ in the limit of elongated droplets $d/h > 1.5$. Data show that this relationship can also be extended to the small droplets when $d/h < 1.5$. The influence of droplet size d with Ca does not significantly alter the value of the aspect ratio d/L since in the thin film regime, L decreases with d [Fig. 3(b)], and in the thick film regime, L increases with d [Fig. 3(c)].

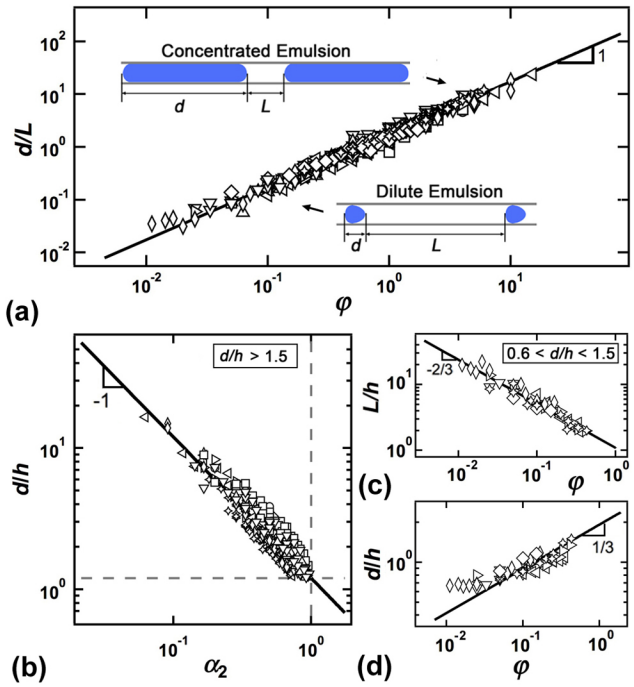

Fig. 4 Dripping regime. (a) Evolution of the multiphase flow linear aspect ratio d/L as a function of flow rate ratio φ, solid line: $d/L = 1.75\varphi$. (b) Concentrated regime ($d/h > 1.5$), droplet length d/h vs. liquid fraction α_2, solid line: $d/h = \alpha_2^{-1}$ (c) Droplet spacing L/h as a function of flow rate ratio φ in the dilute regime ($d/h < 1.5$), solid line: $d/h = 1.1\varphi^{-2/3}$. (d) Droplet length d/h plotted with the flow ratio φ for small droplets, solid line: $d/h = 1.9\varphi^{1/3}$.

In the elongated droplet regime, the normalized droplet size d/h can also be relatively well predicted independently of Ca. Indeed, similar to previous work on the generation of microbubbles,[56] the droplet length can be approximated with $d \sim J \times T_2$ where $J = (Q_1+Q_2)/h^2$ is the superficial flow velocity and $T_2 = (h^3/Q_2)$ is the flow rate-controlled pinching time for breakup. Hence, neglecting the apparent slip velocity between droplet and external phase as well as the weak influence of Ca, the droplet length is expected to be inversely proportional to the continuous phase liquid fraction $\alpha_2 = Q_2/(Q_1+Q_2)$, such as $d/h \sim 1/\alpha_2$. The volumetric fraction α_2 is also a useful parameter for quantifying droplet concentration in segmented flows. Here, the concentrated regime corresponds to a low external phase liquid fraction, $\alpha_2 < 0.8$, and a wide range of elongated droplet sizes can be produced while the droplet spacing remains nearly constant $L \sim h$. By contrast, in the dilute regime ($\alpha_2 > 0.8$), the droplet size remains almost constant $d \sim h$ while the spacing between droplets strongly varies.

In the concentrated droplet regime, data displayed in Fig. 4(b) indicate that the measured droplet size is inversely proportional to the volumetric volume fraction according to

$$\frac{d}{h} = 1.2\alpha_2^{-1} \quad \text{for} \quad \frac{d}{h} > 1.5 \qquad (1)$$

The relative scatter in the data is attributed to the influence of the capillary number Ca on d. In particular, for viscosity ratio $\chi \sim 1$, the previous scaling yields good agreement with experiments when Ca > 1.2×10^{-3}, *i.e.*, in the non-wetting regime. In the wetting regime at very low capillary number, Eq. 1. underestimates the droplet size d/h and previous arguments based on a flow rate-controlled pinching time with no apparent slip between phases do not apply due to the presence of wetting contact lines which alter droplet velocity. Besides data scatter, the previous scaling appears consistent given the wide range of viscosity η_2 variations and the large span of Ca between 10^{-3} and 10^{1}.

The dilute droplet regime is characterized with the emission of small droplets with a fairly narrow size distribution ($0.6 < d/h < 1.5$) while the droplet spacing L varies over a decade. Experimentally, most of our data are produced in the thick film regime. As the droplet spacing L shows a large variation, we measure the size of the liquid plugs of $L2$ between droplets and empirically find a simple scaling such as $L/h \sim \varphi^{-2/3}$ [Fig 4(c)]. Since the linear aspect ratio in the dripping regime is conserved and follows $d/L \sim \varphi$, we obtain the following scaling

$$\frac{d}{h} = 1.9\varphi^{1/3} \quad \text{for} \quad \frac{d}{h} < 1.5, \qquad (2)$$

for the droplet size in the dilute dripping regime, which is associated with small droplets sizes [Fig 4(d)].

3.3 Rivulet regime

The droplet wetting condition can lead to hysteretic behavior and, depending on the history of the system, two modes of droplet formation - dripping and rivulet - are observed for similar input parameters. In the rivulet regime, a wetting tongue of liquid $L1$ can spread on the glass wall past the focusing section and form a rivulet that regularly emits droplets in the outlet channel [Fig. 5(a)]. Once established, the rivulet displays pinned contact lines that are mainly aligned parallel to the flow direction with a static contact angle $\theta < \pi/2$. In this interfacial arrangement, the flow velocity component normal to the contact line is null and the contact angle θ along the rivulet is set independent of the flow capillary number Ca. Progressively increasing the side flow rate Q_2 typically causes the wetting patch to grow further into the microchannel while imposing a sharp variation in Q_2 can revert the system back to the dripping regime.

In the rivulet regime, the relationships for d and L significantly differ from the dripping regime. In particular, we experimentally find that the average distance between droplets L is directly set with the dispersed phase flow rate Q_1. Figure 5(a) shows examples of flows where Q_1 is fixed and Q_2 varies. Monodisperse droplets of various sizes d can be produced at a constant interval L. To better understand this phenomenon, the spacing L/h is meas-

ured from micrographs and found to scale with the flow rate of the droplet phase Q_1 according to $L/h = aQ_1^{-1/2}$, where the coefficient a depends on the particular fluid pair used [Fig. 5(b)]. We apply this method to all fluid pairs and empirically deduce the scaling for the coefficient a as a function of the viscosity ratio χ such as $a = b\chi^{1/4}$ with the constant $b = 29.3$ (μL/min)$^{-1/2}$ [Fig. 5(c)].

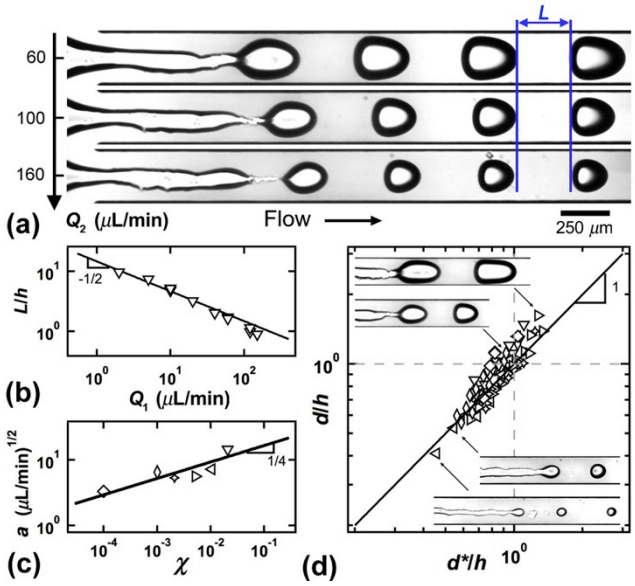

Fig. 5 Rivulet regime. (a) Micrograph showing droplet generation from a rivulet for fixed $Q_1 = 30$ μL/min, fluid pair: W-200cS. The spacing between the droplets L remains constant while Q_2 increases. (b) Evolution of droplet spacing L/h as a function of Q_1 for fluid pair: W-50cS. Solid line: $L/h = aQ_1^{-1/2}$. (c) Evolution of coefficient a with the viscosity ratio χ, solid line: $a = b\chi^{1/4}$. (d) Experimental droplet size d/h as a function of calculated droplet size d^*/h, solid line: $d/h = d^*/h$. Inset: examples of rivulet-generated droplets.

Information about the droplet spacing L allows us to express the scaling for the droplet size d in the rivulet regime. As the droplet size is smaller than the channel height h, it adopts a nearly spherical shape at low Ca and a bullet shape at high Ca. Modeling droplets as spheres during a period of emission gives $(\pi/6)d^3 \sim Q_1$ and using $L \sim Q_2/h^2$ in conjunction with a mass conservation argument leads to $\pi d^3/(6Lh^2) \sim \varphi$. Substituting L with our previous scaling yields a semi-empirical expression for the droplet size d^* in the rivulet regime,

$$\frac{d^*}{h} = \left(b\frac{6}{\pi}\chi^{1/4}Q_1^{1/2}Q_2^{-1} \right)^{1/3}. \qquad (3)$$

The measured droplet size d/h is found to be in good agreement with the proposed scaling d^*/h [Fig. 5(d)]. The bistability observed between the dripping and rivulet production regime is strongly related to local wetting properties of the channel and regime transitions can be triggered with random sessile wetting patches of $L1$ left at the channel walls.

3.4. Dynamic wetting transition

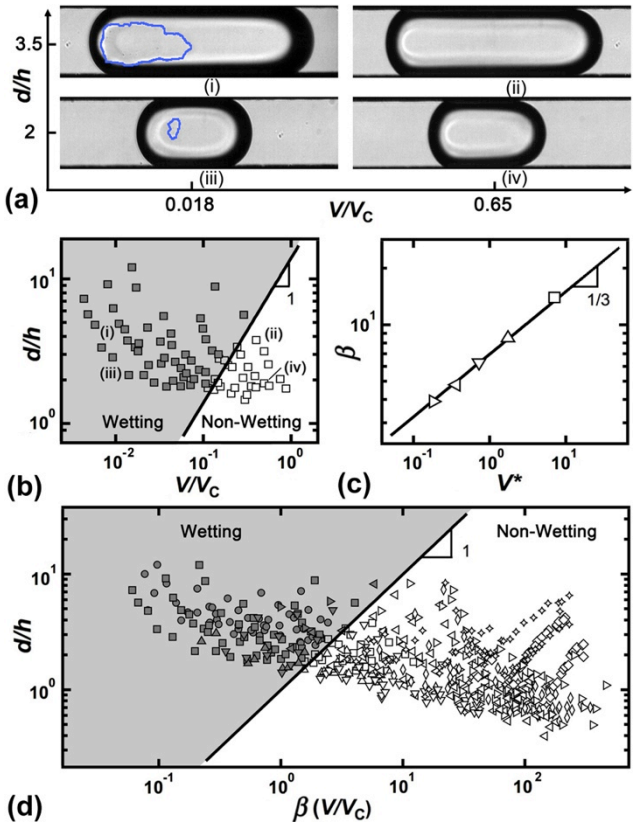

Fig. 6 (a) Experimental micrographs depicting the transition from the wetting to the non-wetting flow regime, contact lines accented (in blue) for visibility, fluid pair: W-5cS. (b) Normalized droplet length d/h vs. rescaled droplet velocity V/V_C, solid line: $d/h = \beta(V/V_C)$ with $\beta = 14$, fluid pair: W-5cS. (d) Evolution of coefficient β with capillary velocity V^* solid line: $\beta = \zeta V^{*1/3}$. (d) Combined wetting phase diagram showing normalized droplet length d/h as a function of $\beta(V/V_C)$ for all fluid pairs. Filled symbols: wetting droplets, open symbols: non-wetting droplets.

For a given fluid pair, the dynamic wetting characteristics of multiphase flows in microchannels depend on the velocity V and size d of droplets [Fig. 6(a)]. The criterion for the wetting transition of translating droplets in pressurized microflows can be determined by comparing the droplet convective timescale $\tau \sim d/V$ with the typical dewetting timescale of the local film based on fluid properties and channel geometry $\tau_D \sim h/V_D$, where V_D is the dewetting velocity. Incidentally, the droplet convective timescale also corresponds to the lifetime of the quasi-static thin film produced by the passage of the droplet at a specific location in the channel. A simple hypothesis for the stability of the thin film associated with a fast lubricated droplet is $\tau \ll \tau_D$. By contrast, unstable thin films are obtained for slow moving droplets with large convective timescales such as $\tau \gg \tau_D$. Balancing timescales and rearranging terms yield an estimate for the wetting transition of microfluidic droplets such as $d/h \sim V/V_D$. For liquid/air system, Redon *et al*[35] showed that the dewetting velocity V_D of a metastable thin film deposited on a sub-

strate is independent of the film thickness δ and scales as $V_D = V^* k\theta_E^3$, where k depends on the nature and on the molecular weight of the liquid.

To test our hypothesis for the droplet wetting transition in microchannels, we inspect flow morphology and map regions of wetting and lubricated droplets on a phase-diagram where d/h is plotted against $V/V_C = Ca/Ca_c$, for a given fluid pair [Fig. 6(b)]. The previous argument yields good agreement with experimental observations as the function $d/h = \beta(V/V_C)$, where the coefficient $\beta = 14$ (for W-5cS), delineates the two regimes. Here, the wetting/non-wetting transition is observed for the five fluid pairs ranging between W-5cS and W-200cS. Since the coefficient $\beta \sim (Ca_c/k\theta_E^3)$ is expected to depend on fluid properties, we plot β as a function of the capillary velocity V^* and find that $\beta = \zeta V^{*1/3}$ with $\zeta = 6.98$ (m/s)$^{-1/3}$ [Fig. 6(c)]. This functional relationship is used to extrapolate the values of β for other fluid pairs and produce a general phase-diagram [Fig. 6(d)] where the line $d/h = \beta(V/V_C)$ clearly separates wetting and non-wetting regimes for all fluid pairs given in Table 1. Hence, the functional relationship

$$\frac{d}{h} = \zeta V^{*1/3}\left(\frac{V}{V_C}\right) \qquad (4)$$

describes the transition between wetting and non-wetting regimes for all cases examined. This equation suggests a critical value for the ratio $d/(h\mathrm{Ca})$ based on the fluid properties of each fluid pair according to $d_{critical}/(h\mathrm{Ca}) = (\zeta V^{*1/3})/Ca_c$. In the diagram, a droplet with the ratio $d/(h\mathrm{Ca}) > (\zeta V^{*1/3})/Ca_c$ belongs to wetting regime. This shows in particular that, similar to the detachment of wetting bubbles between two parallel plates,[57] the droplet wetting transition inside the square capillary can be adjusted with the parameter $d/(h\mathrm{Ca})$.

3.5. Droplet velocity

The evolution of the droplet velocity V is examined for a wide range of size d and capillary number Ca in both the wetting and lubricating flow regimes. The lubricating film has different effects on the droplet velocity in circular and square ducts. In circular capillaries,[58] elongated droplets typically behaves as a tight-fitted piston and moves at about the superficial velocity J. This situation is sometimes referred to as 'plug flow'. In a square channel, the presence of sharp corners introduces non-uniformity in the film thickness and droplets that do not entirely fill the channel cross-section behave as leaky pistons with the presence of a 'corner flow'. The extent of the flow of the continuous phase through the corners sets the relative droplet velocity V/J.[59-63] As the capillary number Ca increases, droplet behavior ranges from a leaky piston in the wetting regime to a fitted piston in the large film thickness δ regimes [Fig. 7(a)].

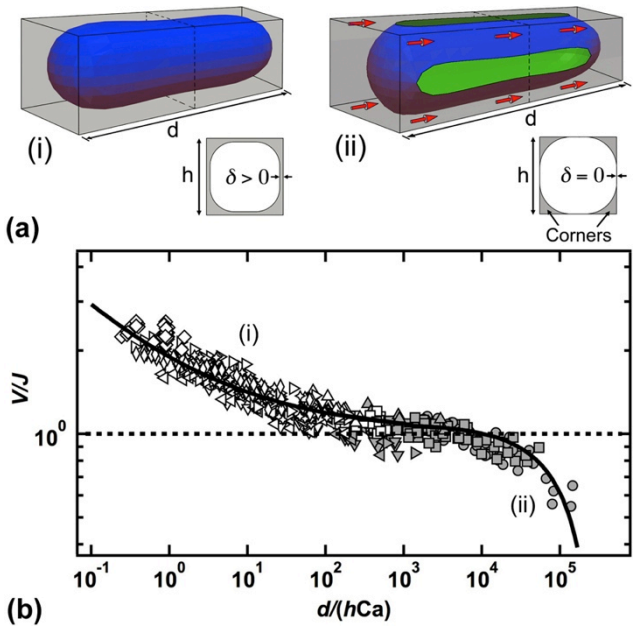

Fig. 7 Droplet velocity. (a) Schematics of an elongated droplet in a square channel as a (*i*) fitted piston and (*ii*) leaky piston with contact line. (b) Normalized droplet velocity V/J plotted as a function of normalized droplet length d/h and capillary number Ca, open symbols: non-wetting droplets, filled symbols: wetting droplets, solid line: $V/J = 1+\xi(d/(h\mathrm{Ca}))^c$, dotted line: $V/J = 1$.

As the wetting transition is essentially controlled with $d/(h\mathrm{Ca})$, this parameter is used to rescale the droplet velocity ratio V/J for all regimes [Fig. 7(b)]. The relative droplet velocity V/J depends on the flux of the continuous phase *L*2 through the four corners in the square microchannel. The corner flux Q_c is proportional to the difference between droplet velocity V and superficial flow velocity J such as $Q_c \sim (V-J)S$, where S is the cross-sectional area of the corners.[64] In the analysis of long bubbles in polygonal capillaries, Wong *et al.*[65] calculated the bubble profile with negligible viscosity and developed an expression for the dependency of corner flux on capillary number and bubble length according to $Q_c \sim (h\mathrm{Ca}^{-1/3}/d)$. In our case with droplets having non-negligible viscosity, however, we find that the expression $Q_c \sim [d/(h\mathrm{Ca})]^c$ allows for rescaling of all data points to a single curve for the range of capillary numbers explored [Fig. 7(b)]. Equating the expressions for Q_c, the ratio of the droplet velocity to the superficial velocity can be written as

$$\frac{V}{J} = 1 + \xi\left(\frac{d}{h\mathrm{Ca}}\right)^c, \qquad (5)$$

where the coefficients ξ and c depend on the droplet wetting condition and are given in Table 2.

Regime	ξ	c
Non-wetting Droplet	9.0×10^{-1}	−1/3
Wetting Droplet	-8.5×10^{-5}	3/4

Table. 2 Fitting parameters of Eq. 5

For a given capillary number Ca, Eq. (5) suggests that, the relative velocity V/J is inversely correlated with the droplet length d, *i.e.*, long droplets move slower. Similarly, when the droplet length d is fixed, the relative velocity increases with the capillary number Ca. For wetting droplets, the direct contact between droplets and the channel walls introduces contact line friction and translating droplets adopt a stick-and-slip behavior and appear as 'reluctant' to move while amounts of the continuous phase bypasses them through corner flows. This behavior is accented in the limit of large $d/(h\mathrm{Ca}) \gg 1$, where the relative droplet velocity $V/J < 1$. There is a transition region for $d/(h\mathrm{Ca})$ in the range of $10^2 \sim 10^3$ where wetting and non-wetting droplets co-exist and the relative velocity is close to unity, $V/J \approx 1$. The coexistence of these two regimes is due to the difference in the wetting criterion given by the critical ratio $d_{\mathrm{critical}}/(h\mathrm{Ca})$ for different fluid pairs.

3.6. Wetting phenomena in square microchannels

Dynamical wetting effects are closely connected to the evolution of the metastable thin film between droplets and channel walls. In our experimental data sets, wetting droplets are observed for a capillary number Ca ranging between 10^{-4} and 10^{-2}. At such low Ca, patches of $L1$ have a tendency to adhere to surfaces and can provide nucleation site for film breakage and growth of a dewetting patch. The temporal evolution of a dewetting patch is shown in Fig 8(a). For very low Ca, a droplet can completely wet the walls, while for moderate Ca near the wetting/thin film transition, partially grown patches are observed at the rear of droplets [Fig 8(b)].

Given the droplet production method where laminar flows of the continuous phase are injected near the sidewalls, wetting effects are more likely to occur at the top and bottom glass surface. At very low Ca, however, wetting effects can be important at the sidewalls. As the silicon surface of the side microchannel is produced during various etching cycles, it is less smooth than the top and bottom glass walls and stick-and-slip motion can result from surface heterogeneities. An example of such motion is shown in Fig. 8(c)(i). Although the average droplet velocity V measured at the centerline remains fairly constant, contact line velocities on the left V_{L} and right V_{R} sidewalls (with respect to the flow direction) show irregular jumps and dips as a moving contact line that encounters a strong surface heterogeneity can pin and relax. This movement consists in intermittent spikes in the normalized velocity of the contact line at both walls [Fig. 8(c)(ii)]. Extraction and superimposition of the contours of a droplet back from high-speed imaging reveal the influence of stick-slip motion on droplet position at fixed time intervals [Fig. 8(c)(iii)].

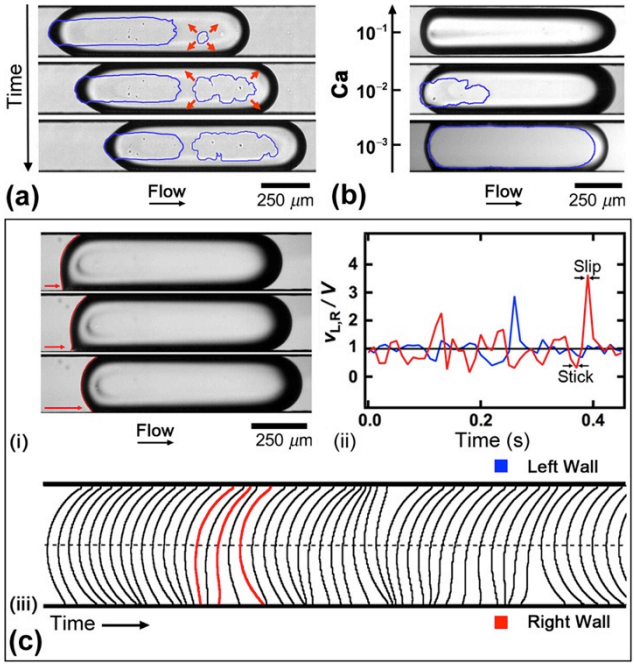

Fig. 8 Examples of wetting dynamics. (a) Time-series of dewetting patch growth during droplet motion, $\Delta t = 4\times10^{-3}$ s. (b) Micrographs showing influence of Ca for fixed d, contact line accented for visibility. (c) Stick and slip motion for V/J = 0.84: (i) Time series of wetting-influenced droplet motion, arrows show pinned and relaxing contact line, $\Delta t = 4\times10^{-3}$, fluid pair W-100cst, (ii) temporal evolution of normalized contact line velocity for left V_L /V and right wall V_R/V and, (iii) super-imposed contours of droplet back illustrating stick-slip motion, contours corresponding to (i) are accented in red.

4. Conclusion

This paper provides a comprehensive study of the rich dynamics of wetting droplets as a function of the viscosity of the external phase in square microchannels. As Ca increases, we delineate four different regimes of intercalating film stability including wetting, thin film, thick film, and constant film regimes. Two coexisting modes of droplet formation - dripping and rivulet – are identified for similar input parameters.

A classification of forced dynamic wetting transitions inside a square microchannel is made in conjunction with information gained on the natural spreading properties of each fluid pair measured using high-speed goniometry. The extrapolated critical wetting velocity V_C for each fluid pair is found proportional to the capillary velocity $V^* = \gamma_{12}/\eta_2$. Comparing droplet dewetting and convective timescales permit categorization of dynamic wetting phenomena in microchannels based on the parameter $d/(h\mathrm{Ca})$, which is also shown to control the relative droplet velocity V/J. A variety of wetting phenomena inside square microchannels, including growth of dewetting patch, droplet morphology, and 'stick-slip' movement of the contact line are also reported. Overall, our study shows the relevance of the dynamic advancing angle as a useful parameter to predict and control wetting transitions of segmented flows in microfluidic platforms.

Acknowledgements

We appreciated discussions with Laurent Limat and Carlos Colosqui. This material is based upon work supported by the National Science Foundation under Grant no. CBET-1150389.

References

1. T. X. Lu, J. W. Biggar and D. R. Nielsen, *Water Resources Research*, 1994, **30**, 3275-3281.
2. C. Pan, M. Hilpert and C. T. Miller, *Water Resources Research*, 2004, **40**.
3. J. Bear, *Dynamics of fluids in porous media*, Elsevier Pub. Co., New York, 1972.
4. S. Basu, K. Nandakumar and J. H. Masliyah, *J Colloid Interf Sci*, 1996, **182**, 82-94.
5. N. Morrow, I. Chatzis and J. Taber, *SPE Reservoir Eng.*, 1988, **3**, 927-934.
6. R. G. dos Santos, R. S. Mohamed, A. C. Bannwart and W. Loh, *J. Petroleum Sci. Eng.*, 2006, **51**, 9-16.
7. E. M. Freer, T. Svitova and C. J. Radke, *J. Petroleum Sci. Eng.*, 2003, **39**, 137-158.
8. H. Foroughi, A. Abbasi, K. S. Das and M. Kawaji, *Phys. Rev. E*, 2012, **85**, 026309.
9. N. M. Kocherginsky, C. L. Tan and W. F. Lu, *J Membrane Sci*, 2003, **220**, 117-128.
10. C. H. Lee, N. Johnson, J. Drelich and Y. K. Yap, *Carbon*, 2011, **49**, 669-676.
11. Z. Shi, W. Zhang, F. Zhang, X. Liu, D. Wang, J. Jin and L. Jiang, *Advanced materials*, 2013, **25**, 2422-2427.
12. S. Litster, D. Sinton and N. Djilali, *J Power Sources*, 2006, **154**, 95-105.
13. G. M. Homsy, *Ann. Rev. Fluid Mech.*, 1987, **19**, 271-311.
14. J. Eggers, *Rev. Mod. Phys.*, 1997, **69**, 865-929.
15. M. J. Blunt, *Curr Opin Colloid In*, 2001, **6**, 197-207.
16. S. Sugiura, M. Nakajima, S. Iwamoto and M. Seki, *Langmuir*, 2001, **17**, 5562-5566.
17. T. M. Squires and S. R. Quake, *Rev. Mod. Phys.*, 2005, **77**, 977-1026.
18. P. Garstecki, H. A. Stone and G. W. Whitesides, *Phys. Rev. Lett.*, 2005, **94**, 164501.
19. A. S. Utada, E. Lorenceau, D. R. Link, P. D. Kaplan, H. A. Stone and D. A. Weitz, *Science*, 2005, **308**, 537-541.
20. G. F. Christopher and S. L. Anna, *J Phys D Appl Phys*, 2007, **40**, R319-R336.
21. T. Cubaud and T. G. Mason, *Phys. Fluids*, 2008, **20**, 053302.
22. T. Ward, M. Faivre and H. A. Stone, *Langmuir*, 2010, **26**, 9233.
23. B. M. Jose and T. Cubaud, *Microfluid. Nanofluid.*, 2012, **12**, 687.
24. M. A. Herrada, A. M. Ganan-Calvo and J. M. Montanero, *Phys. Rev. E*, 2013, **88**, 033027.
25. E. Castro-Hernandez, W. van Hoeve, D. Lohse and J. M. Gordillo, *Lab on a chip*, 2011, **11**, 2023-2029.
26. S. Y. Teh, R. Lin, L. H. Hung and A. P. Lee, *Lab on a chip*, 2008, **8**, 198-220.
27. S. A. Khan, A. Gunther, M. A. Schmidt and K. F. Jensen, *Langmuir*, 2004, **20**, 8604-8611.
28. D. N. Breslauer, P. J. Lee and L. P. Lee, *Molecular Biosystems*, 2006, **2**, 97-112.
29. N. Shahidzadeh-Bonn, A. Tournie, S. Bichon, P. Vie, S. Rodts, P. Faure, F. Bertrand and A. Azouni, *Transport Porous Med*, 2004, **56**, 209-224.
30. F. F. Ouali, G. McHale, H. Javed, C. Trabi, N. J. Shirtcliffe and M. I. Newton, *Microfluid. Nanofluid.*, 2013, **15**, 309-326.
31. T. Cubaud, U. Ulmanella and C.-M. Ho, *Fluid Dyn. Res.*, 2006, **38**, 772-786.

32. P. G. Degennes, *Rev. Mod. Phys.*, 1985, **57**, 827-863.
33. D. Bonn, J. Eggers, J. Indekeu, J. Meunier and E. Rolley, *Rev. Mod. Phys.*, 2009, **81**, 739-805.
34. I. Pászli, I. Mohammed-Ziegler and Z. Hórvölgyi, *Colloid and Polymer Science*, 2007, **285**, 1009-1018.
35. C. Redon, F. Brochard-Wyart and F. Rondelez, *Phys. Rev. Lett.*, 1991, **66**, 715-718.
36. D. Bonn and D. Ross, *Rep Prog Phys*, 2001, **64**, 1085-1163.
37. E. Bertrand, H. Dobbs, D. Broseta, J. Indekeu, D. Bonn and J. Meunier, *Phys. Rev. Lett.*, 2000, **85**, 1282-1285.
38. D. Quéré, *Anu. Rev. Mater Res.*, 2008, **38**, 71.
39. H. Gau, S. Herminghaus, P. Lenz and R. Lipowsky, *Science*, 1999, **283**, 46-49.
40. R. Seemann, M. Brinkmann, E. J. Kramer, F. F. Lange and R. Lipowsky, *P Natl Acad Sci USA*, 2005, **102**, 1848-1852.
41. B. Zhao, J. S. Moore and D. J. Beebe, *Science*, 2001, **291**, 1023-1026.
42. E. B. Dussan and S. H. Davis, *J Fluid Mech*, 1974, **65**, 71.
43. M. Fermigier and P. Jenffer, *J Colloid Interf Sci*, 1991, **146**, 226-241.
44. T. D. Blake and Y. D. Shikhmurzaev, *J Colloid Interf Sci*, 2002, **253**, 196-202.
45. D. Seveno, T. D. Blake, S. Goossens and J. De Coninck, *Langmuir*, 2011, **27**, 14958-14967.
46. S. Goossens, D. Seveno, R. Rioboo, A. Vaillant, J. Conti and J. De Coninck, *Langmuir*, 2011, **27**, 9866-9872.
47. R. G. Cox, *J Fluid Mech*, 1986, **168**, 169.
48. T. D. Blake, *J Colloid Interf Sci*, 2006, **299**, 1-13.
49. N. Le Grand, A. Daerr and L. Limat, *J Fluid Mech*, 2005, **541**, 293-315.
50. R. V. Craster and O. K. Matar, *Rev. Mod. Phys.*, 2009, **81**, 1131.
51. R. Dreyfus, P. Tabeling and H. Willaime, *Phys. Rev. Lett.*, 2003, **90**, 144505.
52. T. Cubaud, M. Fermigier and P. Jenffer, *Oil & Gas Sci. Tech. - Rev. IFP*, 2001, **56**, 23-31.
53. M. J. Madou, *Fundamentals of microfabrication*, CRC Press, Boca Raton, FL, 2002.
54. N. Rashidnia, R. Balasubramaniam and D. Delsignore, *Aiche J*, 1992, **38**, 615-618.
55. O. V. Voinov, *Int. J. Multiphase Flow*, 1995, **21**, 801-816.
56. T. Cubaud, M. Tatineni, X. L. Zhong and C. M. Ho, *Phys. Rev. E*, 2005, **72**.
57. B. Blackmore, D. Q. Li and J. Gao, *J Colloid Interf Sci*, 2001, **241**, 514-520.
58. F. P. Bretherton, *J Fluid Mech*, 1961, **10**, 166-188.
59. H. Wong, C. Radke and S. Morris, *J Fluid Mech*, 1995, **292**, 71-94.
60. M. J. Fuerstman, A. Lai, M. E. Thurlow, S. S. Shevkoplyas, H. A. Stone and G. M. Whitesides, *Lab on a chip*, 2007, **7**, 1479-1489.
61. T. C. Ransohoff and C. J. Radke, *J Colloid Interf Sci*, 1988, **121**, 392-401.
62. P. Parthiban and S. A. Khan, *Biomicrofluidics*, 2013, **7**, 44123.
63. S. A. Vanapalli, A. G. Banpurkar, D. van den Ende, M. H. Duits and F. Mugele, *Lab on a chip*, 2009, **9**, 982-990.
64. C. N. Baroud, F. Gallaire and R. Dangla, *Lab on a chip*, 2010, **10**, 2032-2045.
65. H. Wong, C. J. Radke and S. Morris, *J Fluid Mech*, 1995, **292**, 95-110.